Applied Physics A (2020) 126:621
https://doi.org/10.1007/s00339-020-03805-x

Applied Physics A
Materials Science & Processing

Influence of cooling rate on the magnetic properties of Hf–Co–Fe–B melt-spun alloy

Nithya Christopher[1,2] · Kritika Anand[1,2] · Nidhi Singh[1,2]

Received: 15 April 2020 / Accepted: 13 July 2020 / Published online: 18 July 2020

Abstract

In the present work, $Hf_2Co_{9.5}Fe_{1.5}B$ melt-spun (MS) alloy is synthesized by employing melt spinning at different wheel speeds viz. 16, 20, 24 and 28 m/s to study the effect of quenching on the thermal, structural, microstructural and magnetic properties. The phase purity and the magnetic behaviour of the MS ribbons are highly dependent on the cooling rate that is controlled by altering the tangential wheel speed during melt spinning. Cooling rates are found to increase with increase in wheel speed with a concurrent decrease in the ribbon thickness owing to the increase in the heat transfer coefficient at the thermal contact. The best phase purity and the magnetic properties are found for the ribbons melt-spun at 28 m/s. This could be attributed to the high cooling rate 2.3×10^7 K/s causing crystallization of hard magnetic $Hf_2Co_{11}B$ phase leading to refined grain size. A maximum coercivity (H_C) ~ 2.18 kOe, remanence ratio (M_r/M_s) ~ 0.61, an appreciable magnetic energy product $(BH)_{max}$ ~ 3 MGOe observed in the MS ribbons at 28 m/s illustrates the critical role of wheel speed in the enhancement of permanent magnetic properties in a single-step without annealing. XRD patterns reveal that the alloy was found to crystallize in orthorhombic $Hf_2Co_{11}B$ in addition to cubic Co and Hf_6Co_{23} phases. FE-SEM analysis is carried out to realize the grain morphology and phase identification. The current work exhibits the efficacy of rapid quenching by melt spinning as an effective technique in the development of high-performance $Hf_2Co_{9.5}Fe_{1.5}B$ rare-earth-free permanent magnet alloy for future energy applications in the high-temperature regime.

✉ Nidhi Singh
singhnidhi@nplindia.org

[1] CSIR-National Physical Laboratory, Dr K. S. Krishnan Road, New Delhi 110012, India

[2] Academy of Scientific and Innovative Research (AcSIR), Ghaziabad 201002, India

Graphic abstract

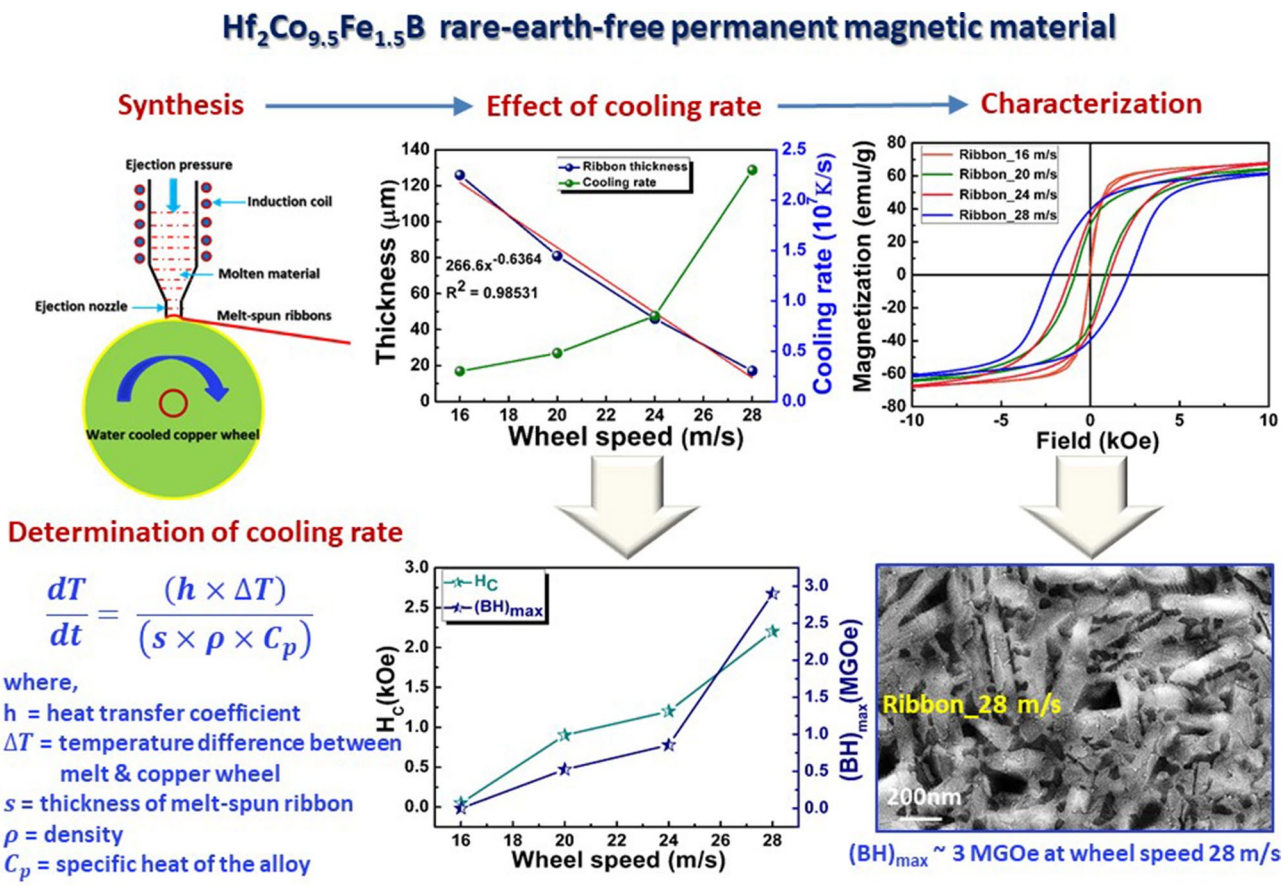

Keywords Melt spinning · Wheel-speed · Cooling-rate · Rare-earth-free permanent magnets

1 Introduction

The global demand for rare-earth resources has led to significant progress in the development of cost-effective rare-earth-free permanent magnet materials with potential use in electric vehicles, wind turbines, etc. [1–4]. In this direction, the scientific community has been focussing on several rare-earth-free permanent magnet materials, as they can be potential substitutes for rare-earth permanent magnets [5–9]. Among the possible materials, Hf-Co based alloys exhibit favourable magnetic properties including high magneto-crystalline anisotropy (K_1) ~ 10 Mergs cm^{-3}, high Curie temperature (T_C) ~ 477–497 °C and high magnetic polarization (J_s) ~ 10 kG ($J_s = 4\pi M_s$) [10–13] that are associated with the presence of $HfCo_7$ or Hf_2Co_{11} hard magnetic phases [11, 14–18]. $HfCo_7$ crystallizes in orthorhombic structure, while Hf_2Co_{11} crystallizes in rhombohedral and orthorhombic crystal structures [17], yet structural similarity between these phases have been reported earlier [19].

Hf–Co based alloys have been widely studied as an important class of rare-earth-free permanent magnet material [9–11, 13, 14, 16–30]. However, multi-step synthesis process including complex heat treatments and mechanical alloying are requisite for the enhancement of permanent magnetic properties [13, 18, 23, 29, 31–33]. Several experimental studies on melt spinning [13, 17, 18, 23, 34–37] reveal that the evolution of hard magnetic behaviour in this class of alloys is strongly annealing dependent. The experimental investigation on variation in wheel speed is reported only by McGuire et al. on the synthesis of $Hf_2Co_{11}B$ alloys to obtain magnetically hard nanocrystalline phases [11]. The crystallization process in $Hf_2Co_{11}B$ melt-spun (MS) alloy at different heating rates is studied by Musial et al. using DSC measurements and reported an enhanced glass-forming ability (GFA) in Hf–Co–B system [24]. A computational study based on Miedema's model reported a low GFA in Cr–Co–B system in comparison to Hf–Co–B system [25]. Hf–Co alloys are structurally

metastable through non-equilibrium conditions during melt spinning. Hence, the synthesis of the nanostructured Hf–Co alloys by altering the wheel speed remains a challenging issue.

Melt spinning is one of the widely used rapid solidification technique to produce hard magnetic ribbons for permanent magnets. In this technique, a melted liquid alloy is ejected out of the nozzle and directed onto the surface of a rotating copper wheel, where the liquid jet is rapidly solidified into a continuous thin ribbon. The rapid heat extraction during quenching consist of both superheat and latent heat [22, 38]. The rapid solidification phenomena play a key role in the determination of microstructure of the metastable phases and consequently the magnetic properties of the alloy [16]. Melt spinning processing parameters, such as, wheel speed, gas ejection pressure, melt temperature, ejection temperature and slit nozzle-wheel distance, etc. control the thickness of the ribbons that largely determine the cooling rate [39]. Among them, wheel speed is the most important parameter that primarily influences the cooling rate of the melt-spun ribbons.

In our previous work of Hf–Zr–Co–Fe–B MS alloy, we found that the optimized annealing protocol of the ribbons resulted in the evolution of hard magnetic phases $Hf_2Co_{11}B$ and $ZrCo_{5.1}$ leading to the enhancement of permanent magnetic properties [23]. Herein, we report an optimized single-step synthesis route without annealing to develop microstructural and magnetic properties under non-equilibrium conditions employing melt spinning at a varied cooling rate. The tangential velocity of the melt spinning wheel was altered to achieve different cooling rates resulting in varying ribbon thickness.

In the current study, we report $(BH)_{max}$ ~ 3 MGOe at room temperature in an optimized composition of $Hf_2Co_{9.5}Fe_{1.5}B$ MS ribbons at the highest wheel speed. This enhancement in $(BH)_{max}$ is due to the synergistic integration of high cooling rate and nanostructuring for obtaining hard magnetic $Hf_2Co_{11}B$ phase, which leads to an enhanced coercivity and remanence and the favourable tuning of permanent magnetic properties. Thermal characteristics of the synthesized MS ribbons at varying wheel speed is estimated using the DSC analysis. The MS ribbons were structurally characterized employing XRD and FE-SEM, based on which the enhancement of the $(BH)_{max}$ has been discussed.

2 Experimental

High purity (99.99%) elements of Hf, Co, Fe and B were repeatedly arc-melted employing mini arc-melter (MAM-1, Edmund Buhler GmbH) under vacuum to obtain an ingot with uniform composition. The ingot was then melt-spun employing Melt-spinning unit (Melt Spinner HV, Edmund Buhler GmbH) at different wheel speeds of 16–28 m/s under a vacuum of ~ 10^{-6} mbar. The maximum wheel speed of 28 m/s was attainable employing the existing equipment. The resultant MS ribbons were about 20–30 cm long, 0.5–1 cm wide and 17–126 µm thick depending upon the cooling rate. The thickness of the MS ribbons was measured using Mitutoyo Digimatic Micrometer. Thermal analysis was performed using differential scanning calorimeter (DSC, 404 F3 Pegasus, Netzch) to identify the phase transition temperatures. Phase formation and phase purity of the samples were characterized using the Powder X-Ray Diffraction (XRD, Rigaku-Miniflex, CuKα1, 1.5406 Å). Microstructural characterization was carried out using Field Emission Scanning Electron Microscopy (FE-SEM, Carl Zeiss Supra 40VP). The magnetic properties were measured using a Vibrating Sample Magnetometer (Lakeshore, VSM 7410).

3 Results and discussion

3.1 Thermal transformations

Figure 1 exhibits the DSC curves of the MS ribbons at different cooling rates (corresponding to the wheel speed of ~ 16, 20, 24 and 28 m/s), measured at a heating rate of 10 K/min. Two exothermic peaks T_1 and T_2 were observed for the ribbons melt-spun at 16 m/s, at 604.9 and 640.3 °C which corresponds to the crystallization of orthorhombic $Hf_2Co_{11}B$ phase and the decomposition of metastable phases, respectively [22, 40]. Whereas for the ribbons melt-spun at higher cooling rates (for wheel speed of 20, 24 and 28 m/s), no exothermic peaks were observed. This suggests that higher cooling rates of as melt-spun ribbons result in the formation of crystalline phases in a single-step.

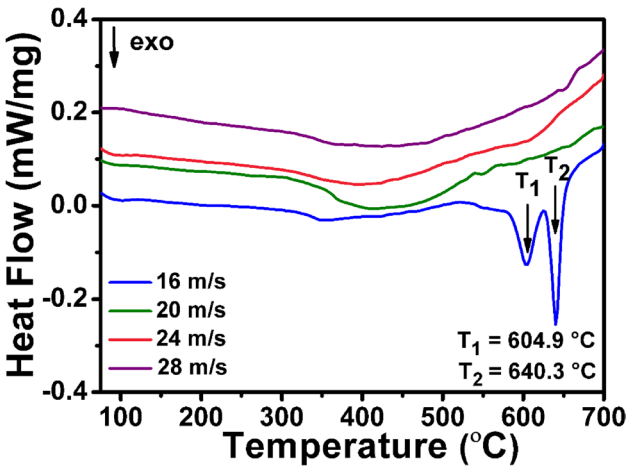

Fig. 1 DSC thermograms of $Hf_2Co_{9.5}Fe_{1.5}B$ MS alloy at a heating rate of 10 K/min

3.2 Phase analysis

Figure 2 displays the XRD patterns of the arc-melted ingot and as-spun ribbons synthesized at different wheel speeds ranging from 16 to 28 m/s. The XRD pattern of the arc-melted alloy corresponds to orthorhombic $Hf_2Co_{11}B$, cubic Co (JCPDS No. 00-001-1259) and $HfCo_3B_2$ (JCPDS No. 00-022-0220) phases. Also observed was the reflection from the cubic Co close to those of $HfCo_3B_2$ in the 2θ range between 42 and 44°. For the wheel speed of 16 m/s, peaks and humps were present together, illustrating the coexistence of amorphous and crystalline phases. Sharp crystalline peaks were observed for the ribbons melt-spun at 20 m/s indicating good crystallinity. These peaks were indexed to orthorhombic $Hf_2Co_{11}B$, cubic Co and Hf_6Co_{23} phases. It was also observed that the orthorhombic $Hf_2Co_{11}B$ phase at 44.2° overlaps with the peak position of cubic Co complicating the phase identification. Additionally, with the increase in wheel speed, an increase in the peak intensity of Hf_6Co_{23} observed along with $Hf_2Co_{11}B$, fcc Co and $HfCo_3B_2$ phases. These results confirm that a higher cooling rate favours the formation of multiple phases, leading to enhanced exchange coupling between these phases contributing to a significant increase in the remanence ratio to 0.61. Melt spinning at 16 m/s showed partially crystalline ribbons, while at 28 m/s the ribbon was found to be completely crystalline. XRD analysis concludes that crystallization stems from higher cooling rate, due to the formation of hard magnetic phases, which is in accordance with the DSC analysis.

3.3 Dependence of ribbon thickness on cooling rate

Figure 3 shows the variation of ribbon thickness and cooling rate as a function of wheel speed. The fitted curve is obtained from the regression analysis with a correlation factor (R^2) of 0.985, which signifies that ribbon thickness is inversely proportional to the wheel speed. The melt layer concomitantly influenced by the increasing wheel speed and the centrifugal force will rapidly move away from the rotating wheel, thereby reducing the ribbon thickness. Figure 3 also illustrates the functional dependence of ribbon thickness on wheel speed according to the ideal cooling theory [41]. When the melt layer on the wheel surface is thinner, the entire layer will be undercooled resulting in high cooling rate through the entire transverse cross section of the ribbon. Whereas, for a thicker melt layer, solidification at the contact surface starts before the entire layer is undercooled and the crystallization heat absorbed by the remaining melt will decrease its cooling rate. Hence, the ribbons with thickness ~ 17 µm show clear evidence of high cooling rate ~ 2×10^7 K/s, while the ribbons ~ 126 µm shows low cooling rate ~ 3×10^6 K/s. The cooling rate is determined from the equation:

$$\frac{dT}{dt} = \frac{h \times \Delta T}{s \times \rho \times C_p}$$

where h is the heat transfer coefficient, ΔT is the difference between the melt temperature and the temperature of the copper wheel, s is the thickness of the melt-spun ribbon, ρ is the density of the material and C_p is the specific heat of the material. These experimental data concludes that the increase in wheel speed leads to a decrease in ribbon

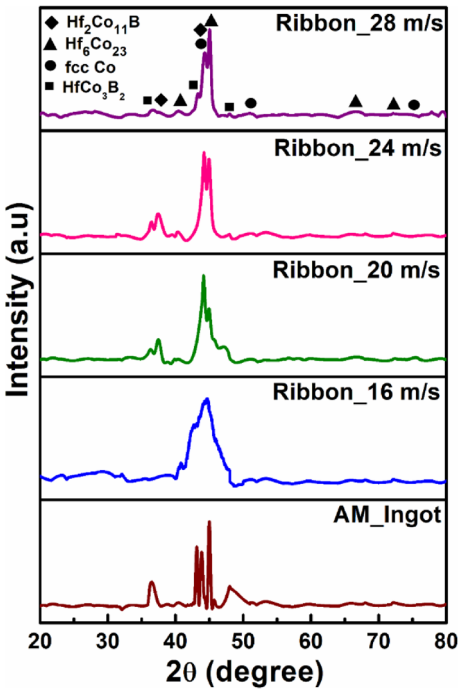

Fig. 2 XRD patterns of $Hf_2Co_{9.5}Fe_{1.5}B$ arc-melted ingot and ribbons melt-spun at various wheel speeds

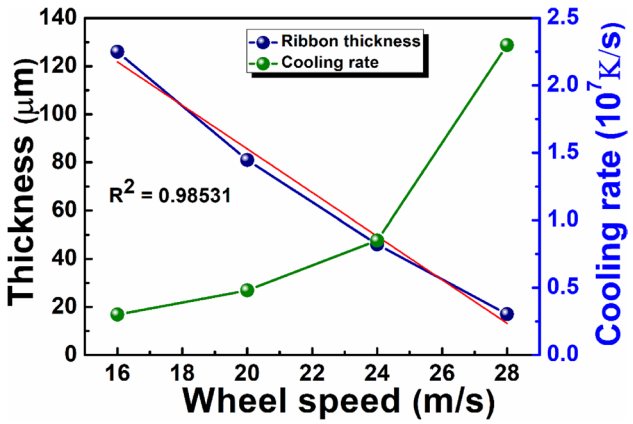

Fig. 3 Variation of ribbon thickness with cooling rate of $Hf_2Co_{9.5}Fe_{1.5}B$ MS alloy

thickness as well as enhance the heat transfer coefficient at the wheel-ribbon interface [38].

3.4 Microstructural analysis

The morphology of the arc-melted ingot and as grown MS ribbon synthesized at an optimized high cooling rate of ~ 2×10^7 K/s corresponding to the wheel speed of 28 m/s were investigated employing FE-SEM. As can be seen in Fig. 4a, the microstructure of the arc-melted alloy composed of fine lamellar microstructures (denoted as A) displaying an average composition close to the starting composition ($Hf_2Co_{9.5}Fe_{1.5}B$). Furthermore, a light grey region (denoted as B) contained Fe in lesser concentration in comparison to the starting composition and dark grey region (denoted as C) are pockets of Co dispersed all over the matrix. When the arc-melted alloy was rapidly quenched at an optimized high cooling rate of ~ 2×10^7 K/s, the as-spun ribbons thus obtained exhibit flower-like nanostructures (Fig. 4b) composed of nanorods (Fig. 4c). These nanorods were found to have a diameter of about 50–200 nm and a length of about 0.7–1.5 µm. Large arrays of these nanorods with controlled morphology plays a key role in enhancing the coercivity and remanence in $Hf_2Co_{9.5}Fe_{1.5}B$ alloy.

3.5 Magnetization measurements

Figure 5a exhibits the room temperature magnetic hysteresis (M–H) loops of the arc-melted ingot and the as MS ribbons of $Hf_2Co_{9.5}Fe_{1.5}B$ synthesized at different wheel speeds. The

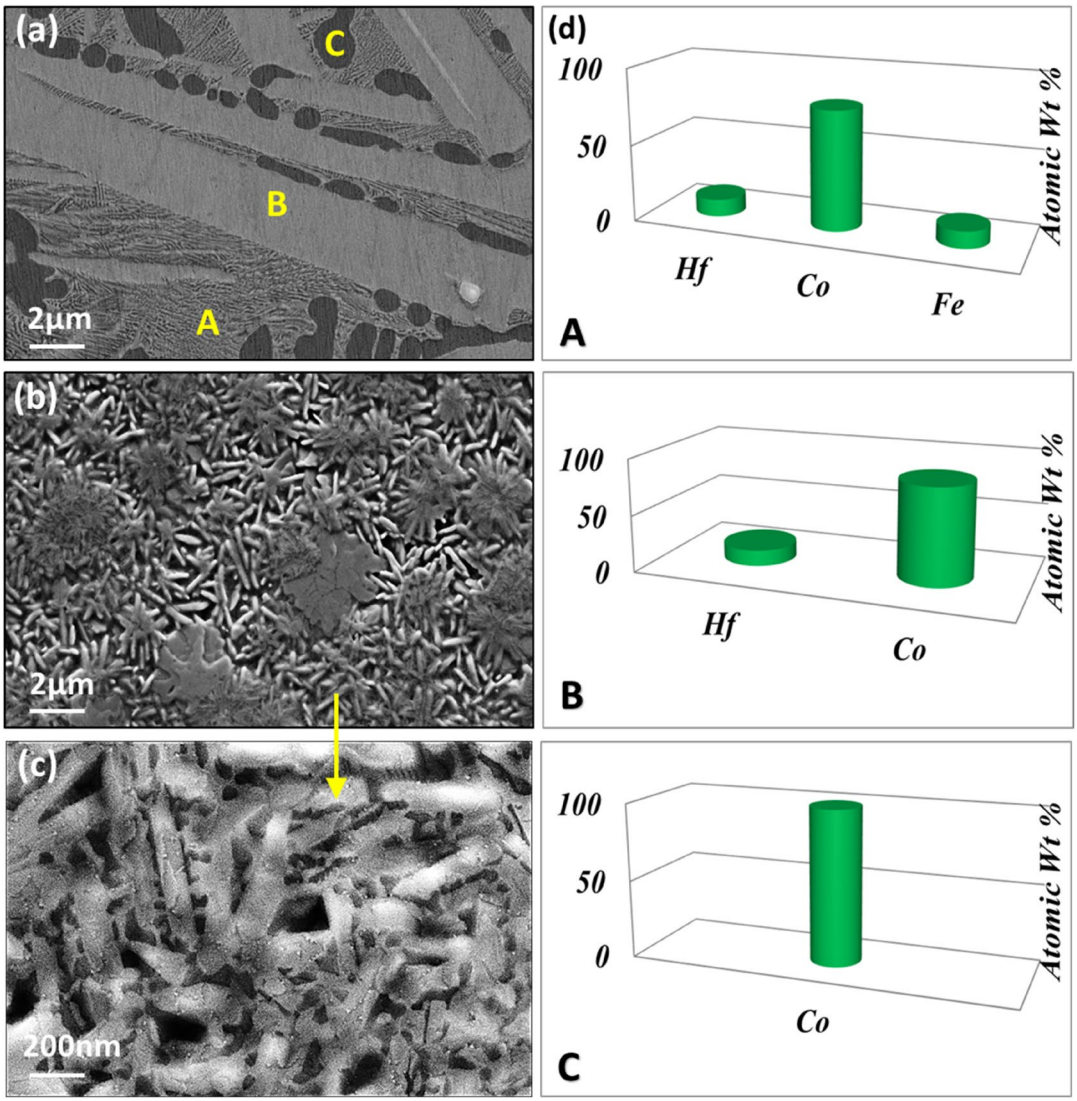

Fig. 4 FE-SEM images of **a** arc-melted ingot, **b** and **c** MS ribbon at a high cooling rate 2.3×10^7 K/s and **d** EDAX analysis of marked regions in (**a**) of $Hf_2Co_{9.5}Fe_{1.5}B$ MS alloy

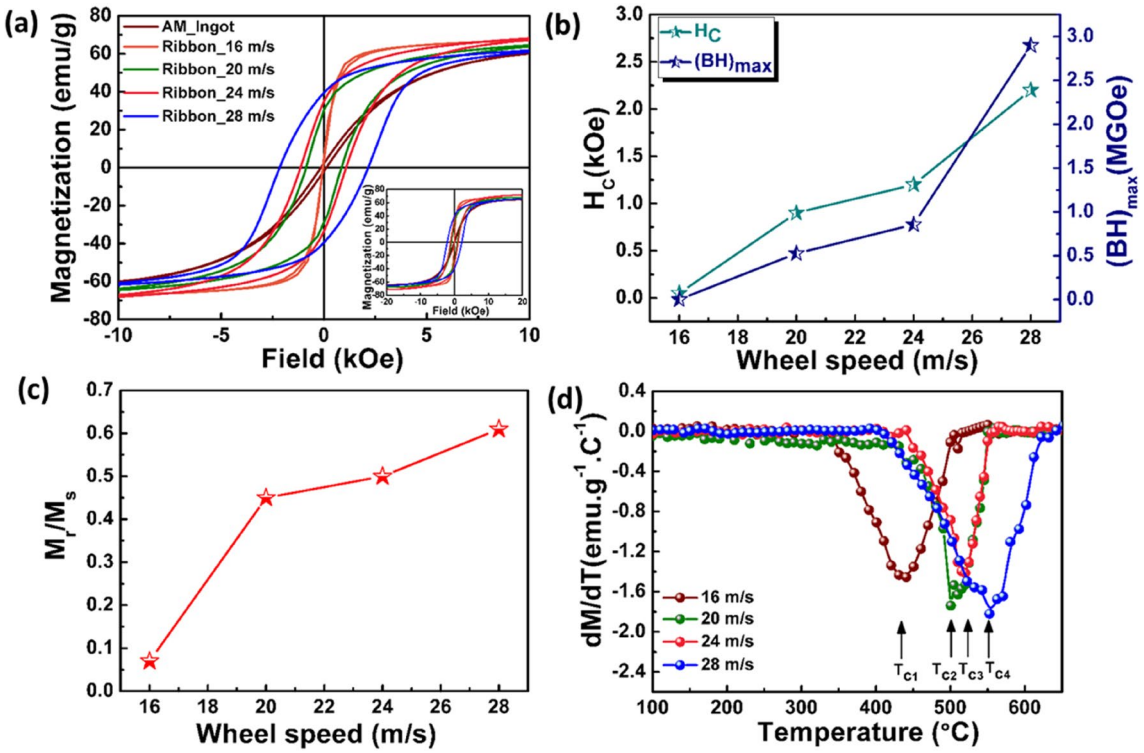

Fig. 5 Effect of wheel speed on **a** M–H curves, **b** H_C and $(BH)_{max}$, **c** (M_r/M_s) ratio, at room temperature and **d** dM/dt vs. T curves, of $Hf_2Co_{9.5}Fe_{1.5}B$ MS alloy

inset of the figure shows the same in extended field region up to 2 T. The magnetic parameters determined from the (M–H) loops are presented in Table 1. It can be observed that the ribbons melt-spun at 16 m/s displays better magnetic properties as compared to their arc-melted counterpart. A high saturation magnetization $(M_s) \sim 67.31$ emu/g and a low $(H_C) \sim 0.009$ kOe was realized for the ribbons melt-spun at a low wheel speed of 16 m/s. This is in agreement with the XRD analysis of the ribbons (Fig. 2) which displays a broad feature centred near 44°, illustrating the alloy quenched at lower wheel speed, 16 m/s ($\sim 3 \times 10^6$ K/s) are partially crystalline. However, upon a further increase in the wheel speed, significant crystallization of hard magnetic $Hf_2Co_{11}B$ phase as evident from XRD pattern increases the coercivity, remanence and magnetic energy product as observed in Fig. 5b, c. A maximum $(BH)_{max} \sim 2.93$ MGOe, $({}_iH_C) \sim 2.2$ kOe and (M_r/M_s) over 0.5 was achieved in $Hf_2Co_{9.5}Fe_{1.5}B$ MS ribbons synthesized at a high cooling rate $\sim (2.3 \times 10^7$ K/s) corresponding to the wheel speed of 28 m/s. The enhancement of hard magnetic properties at a higher cooling rate primarily originates from the hard magnetic nanocrystalline microstructure.

The Curie temperatures of the ribbons melt-spun at different wheel speeds were obtained from the first-order derivative dM/dT as shown in Fig. 5d. A shift in the Curie temperature is observed in the melt-spun samples with the increasing wheel speed. This effect is attributed to the presence of the different amount of boron incorporated in the nanocrystalline phases formed during melt spinning [17, 42]. In the present study, the highest (T_C) was achieved in

Table 1 Magnetic parameters of $Hf_2Co_{9.5}Fe_{1.5}B$ samples obtained from hysteresis loops

Synthesis conditions	Wheel speed (m/s)	Thickness of ribbons (μm)	Cooling rate (K/s)	M_s (emu/g)	M_r (emu/g)	H_C (kOe)	$(BH)_{max}$ (MGOe)
Ingot	–	–	–	64.12	2.32	0.15	0.0004
MS ribbon	16	126	3×10^6	67.31	4.90	0.009	–
MS ribbon	20	81	4.8×10^6	67.64	30.38	0.88	0.53
MS ribbon	24	46	8.5×10^6	71.12	35.63	1.15	0.86
MS ribbon	28	17	2.3×10^7	65.36	39.69	2.18	2.94

the fully crystalline sample at 552 °C ($Hf_2Co_{11}B$), corresponding to the wheel speed of 28 m/s. These results are in accordance with the similar work reported for $Hf_2Co_{11}B$ MS alloy, where the curie temperatures of both amorphous and crystalline samples are near 497 °C [11].

4 Conclusion

In the present work, we have explored melt spinning technique to understand the influence of cooling rate on the thermal, microstructural and magnetic properties at an optimized composition of $Hf_2Co_{9.5}Fe_{1.5}B$ melt-spun alloy. The cooling rate is altered by tuning the tangential wheel speed during melt spinning. It was found that the cooling rate in the vicinity of the melt temperature increases from 3×10^6 to 2.3×10^7 K/s by increasing the wheel speed from 16 to 28 m/s, while the ribbon thickness decreases from 126 to 17 μm. At the highest cooling rate, the evolution of hard magnetic $Hf_2Co_{11}B$ phase with $(H_C) \sim 2.2$ kOe, $(M_r/M_s) \sim 0.61$ and $(BH)_{max} \sim 3$ MGOe has been obtained in the fully crystalline sample. XRD analysis confirms that crystallization stems from higher cooling rate by the evolution of hard magnetic phases, which is in accordance with the DSC analysis. The microstructure of the optimized sample consists of flower-like nanostructures with a large array of nanorods responsible for high coercivity and remanence. These experimental results gain an insight into the strong dependence of cooling rate on the magnetic characteristics. The present study evaluates the significance of the optimization of cooling rate resulting in the direct crystallization of hard magnetic phase in a single-step without the need for annealing. Greater homogeneity, extended solid solubility, refinement of grain size and better control of the desired hard magnetic phases contributes to the substantial enhancement of $(BH)_{max}$. Further optimization of melt-spin parameters will form the basis for future studies on the enhancement of the magnetic energy product and high magnetic performance. Thus, the synthesized $Hf_2Co_{9.5}Fe_{1.5}B$ MS alloy could be a potential candidate for rare-earth-free permanent magnet in the future energy applications in the high-temperature regime.

References

1. D. Goll, R. Loeffler, J. Herbst, R. Karimi, G. Schneider, High-throughput search for new permanent magnet materials. J. Phys. Condens. Matter **26**, 064208 (2014)
2. M. Kuz'Min, K. Skokov, H. Jian, I. Radulov, O. Gutfleisch, Towards high-performance permanent magnets without rare earths. J. Phys. Condens. Matter **26**, 064205 (2014)
3. J. Coey, Hard magnetic materials: a perspective. IEEE Trans. Magn. **47**, 4671–4681 (2011)
4. F. Ronning, S. Bader, Rare earth replacement magnets. J. Phys. Condens. Matter **26**, 060301 (2014)
5. B. Balasubramanian, B. Das, R. Skomski, W.Y. Zhang, D.J. Sellmyer, Novel nanostructured rare-earth-free magnetic materials with high energy products. Adv. Mater. **25**, 6090–6093 (2013)
6. N.R. Christopher, N. Singh, S.K. Singh, B. Gahtori, S. Mishra, A. Dhar, V. Awana, Appreciable magnetic moment and energy density in single-step normal route synthesized MnBi. J. Supercond. Novel Magn. **26**, 3161–3165 (2013)
7. T. Gao, Y. Wu, S. Fackler, I. Kierzewski, Y. Zhang, A. Mehta, M. Kramer, I. Takeuchi, Combinatorial exploration of rare-earth-free permanent magnets: magnetic and microstructural properties of Fe–Co–W thin films. Appl. Phys. Lett. **102**, 022419 (2013)
8. W. Zhang, X. Li, S. Valloppilly, R. Skomski, J.E. Shield, D.J. Sellmyer, Magnetism of rapidly quenched rhombohedral Zr2Co11-based nanocomposites. J. Phys. D Appl. Phys. **46**, 135004 (2013)
9. B. Balasubramanian, P. Mukherjee, R. Skomski, P. Manchanda, B. Das, D.J. Sellmyer, Magnetic nanostructuring and overcoming Brown's paradox to realize extraordinary high-temperature energy products. Sci. Rep. **4**, 6265 (2014)
10. M.C. Nguyen, L. Ke, X. Zhao, V. Antropov, C.-Z. Wang, K.-M. Ho, Atomic structure and magnetic properties of HfCo7 alloy. IEEE Trans. Magn. **49**, 3281–3283 (2013)
11. M.A. McGuire, O. Rios, N.J. Ghimire, M. Koehler, Hard ferromagnetism in melt-spun Hf2Co11B alloys. Appl. Phys. Lett. **101**, 202401 (2012)
12. H. Chang, M. Liao, C. Shih, W. Chang, C. Yang, C. Hsiao, H. Ouyang, Hard magnetic property enhancement of Co7Hf-based ribbons by boron doping. Appl. Phys. Lett. **105**, 192404 (2014)
13. A. Musiał, Z. Śniadecki, B. Idzikowski, Development of magnetic properties during annealing of Hf2Co11B amorphous alloy. Acta Phys. Pol., A **131**, 786–788 (2017)
14. X.-Z. Li, Y.-L. Jin, M.-Y. Wang, J. Shield, R. Skomski, D.J. Sellmyer, Electron diffraction study of cobalt-rich Hf–Co. Intermetallics **75**, 54–61 (2016)
15. I. Singh, M. Palit, H. Basumatary, R. Mathur, M. Joseph, Microstructural evolution and magnetic properties of Co-rich Hf–Co alloys. J. Alloy. Compd. **763**, 742–748 (2018)
16. B. Balamurugan, B. Das, W. Zhang, R. Skomski, D.J. Sellmyer, Hf–Co and Zr–Co alloys for rare-earth-free permanent magnets. J. Phys. Condens. Matter **26**, 064204 (2014)
17. A. Musiał, Z. Śniadecki, J. Marcin, J. Kováč, I. Škorvánek, B. Idzikowski, Magnetism of coexisting rhombohedral and orthorhombic Hf2Co11 phases in rapidly quenched Hf2Co11B. J. Alloy. Compd. **665**, 93–99 (2016)
18. M.A. McGuire, O. Rios, Evolution of magnetic properties and microstructure of Hf2Co11B alloys. J. Appl. Phys. **117**, 053912 (2015)
19. B. Demczyk, S. Cheng, Structures of Zr2Co11 and HfCo7 intermetallic compounds. J. Appl. Crystallogr. **24**, 1023–1026 (1991)
20. I.A. Al-Omari, W. Zhang, L. Yue, R. Skomski, J.E. Shield, X. Li, D.J. Sellmyer, Hf doping effect on hard magnetism of nanocrystalline Zr18–xHfxCo82 Ribbons. IEEE Trans. Magn. **49**, 3394–3397 (2013)
21. B. Das, B. Balamurugan, P. Kumar, R. Skomski, V. Shah, J.E. Shield, A. Kashyap, D.J. Sellmyer, HfCo7-based rare-earth-free permanent-magnet alloys. IEEE Trans. Magn. **49**, 3330–3333 (2013)
22. X. Lu, K. Cheng, S. Liu, K. Li, F. Zheng, Y. Du, Experimental investigation of phase equilibria in the Co–Hf system. J. Alloy. Compd. **627**, 251–260 (2015)
23. N. Christopher, K. Anand, A. Srivastava, A. Gupta, N. Singh, Microstructure versus magnetic properties correlations in melt-spun Hf–Zr–Co–Fe–B alloys: role of thermal treatment. Mater. Res. Express **5**, 066104 (2018)

24. A. Musiał, Z. Śniadecki, B. Idzikowski, Thermal stability and glass forming ability of amorphous Hf2Co11B alloy. Mater. Des. **114**, 404–409 (2017)
25. Z. Śniadecki, A. Musiał, A.R. Kilmametov, Glass forming ability of (Hf, Cr) CoB alloys: computational and experimental studies. Mater. Charact. **132**, 46–52 (2017)
26. M.A. McGuire, R. Orlando, N.J. Ghimire, Hf–Co–B alloys as permanent magnet materials. Google Patents (2017).
27. J. Belošević-Čavor, F. Congiu, V. Koteski, B. Cekić, G. Concas, Magnetism of the compounds in the Hf–Co phase system. Mater. Sci. Forum **518**, 319–324 (2006)
28. D. Sellmyer, B. Balamurugan, W. Zhang, B. Das, R. Skomski, P. Kharel, Y. Liu, Advances in rare-earth-free permanent magnets. Proceedings of the 8th Pacific Rim international congress on advanced materials and processing, Springer, 2013, pp. 1689–1696.
29. G.D. Yüzüak, E. Yüzüak, Y. Elerman, Hf2Co11 thin films: rare-earth-free permanent nanomagnets. Thin Solid Films **625**, 115–121 (2017)
30. J.A. Lewis, Structural & magnetic characterization study of hfco7 alloy with substitutions of Si, Ti, Fe, Mn & B. Mechanical (and Materials) Engineering -- Dissertations, Theses, and Student Research 64, (2013). https://digitalcommons.unl.edu/mechengdiss/64
31. N. Kataoka, K. Suzuki, A. Inoue, T. Masumoto, Magnetic properties of iron-base bcc alloys produced by mechanical alloying. J. Mater. Sci. **26**, 4621–4625 (1991)
32. A. Musiał, Z. Śniadecki, N. Pierunek, Y. Ivanisenko, D. Wang, M. Fawey, B. Idzikowski, Tuning of the magnetic properties of Hf2Co11B alloys through a combined high pressure torsion and annealing treatment. J. Alloy. Compd. **787**, 794–800 (2019)
33. A. Musiał, J. Kováč, Z. Śniadecki, Magnetic properties of Hf2 (Fe_xCo_{1-x}) 11B ($x = 02, 04$) alloys synthesized from structurally metastable phases. J. Magn. Magn. Mater. **514**, 167008 (2020)
34. A.M. Gabay, G.C. Hadjipanayis, J. Cui, New anisotropic MnBi permanent magnets by field-annealing of compacted melt-spun alloys modified with Mg and Sb. J. Magn. Magn. Mater. **495**, 165860 (2020)
35. S. Kim, H. Moon, H. Jung, S.-M. Kim, H.-S. Lee, H. Choi-Yim, W. Lee, Magnetic properties of large-scaled MnBi bulk magnets. J. Alloy. Compd. **708**, 1245–1249 (2017)
36. M. Szwaja, P. Gębara, J. Filipecki, K. Pawlik, A. Przybył, P. Pawlik, J.J. Wysłocki, K. Filipecka, Influence of Nb addition on vacancy defects and magnetic properties of the nanocrystalline Nd–Fe–B permanent magnets. J. Magn. Magn. Mater. **382**, 307–311 (2015)
37. A. Przybył, K. Pawlik, P. Pawlik, P. Gębara, J. Wysłocki, Phase composition and magnetic properties of (Pr, Dy)–Fe–Co–(Ni, Mn)–B–Zr–Ti alloys. J. Alloy. Compd. **536**, S333–S336 (2012)
38. V.I. Tkatch, S.N. Denisenko, O.N. Beloshov, Direct measurements of the cooling rates in the single roller rapid solidification technique. Acta Mater. **45**, 2821–2826 (1997)
39. R. Mehrabian, Rapid solidification. Int. Metals Rev. **27**, 185–208 (1982)
40. A. Musial, Z. Śniadecki, J. Marcin, J. Kovac, I. Škorvánek, B. Idzikowski, Magnetism of coexisting rhombohedral and orthorhombic Hf2Co11 phases in rapidly quenched Hf2Co11B. J. Alloys Compd. **665**, 93–99 (2015)
41. R. Budhani, T. Goel, K. Chopra, Melt-spinning technique for preparation of metallic glasses. Bull. Mater. Sci. **4**, 549–561 (1982)
42. W. Zhang, S. Valloppilly, X. Li, Y. Liu, S. Michalski, T. George, R. Skomski, D.J. Sellmyer, Magnetic hardening of Zr2Co11: (Ti, Si) nanomaterials. J. Alloy. Compd. **587**, 578–581 (2014)